

Supporting information for

Tailoring the Desorption Behavior of Hygroscopic Gels for Atmospheric Water Harvesting in Arid Climates

Hengyi Lu, Wen Shi, James H. Zhang, Amylynn C. Chen , Weixin Guan, Chuxin Lei, Julia R. Greer, Svetlana V. Boriskina, and Guihua Yu*

H. Lu, W. Shi, W. Guan, C. Lei, Prof. G. Yu
Materials Science and Engineering Program and Walker Department of Mechanical Engineering,
The University of Texas at Austin, Austin, TX 78712, USA
Email: ghyu@austin.utexas.edu

J. Zhang, Dr. S. V. Boriskina
Department of Mechanical Engineering, Massachusetts Institute of Technology, Cambridge, MA
02139, USA

A. Chen, Prof. J. R. Greer
Division of Engineering and Applied Science, California Institute of Technology, Pasadena, CA
91125, USA

S1. Supplementary Methods

- S1.1 Chemicals and materials
- S1.2 Synthesis and Fabrication
- S1.3 Characterizations
- S1.4 Water collection experiments
- S1.5 Molecular dynamic simulations

S2. Supplementary Figures and Tables

- S2.1 Microscopic observation of PAM-LiCl
- S2.2 Mechanical property of PAM-LiCl
- S2.3 Water sorption performance of uncrosslinked PAM-LiCl, PVA-LiCl and PAA-LiCl
- S2.4 Optimizing the Li content in PAM-LiCl
- S2.5 Water sorption isotherm of PAM gel
- S2.6 Sorption performance comparison between PAM-LiCl and literature
- S2.7 Salt leakage prevention effects of PAM-LiCl
- S2.8 Water sorption and desorption rate of PAM-LiCl and LiCl
- S2.9 Desorption heat PAM-LiCl and LiCl
- S2.10 Freezable water content in PAM-LiCl and LiCl
- S2.11 Evaluation of heat of sorption of PAM-LiCl
- S2.12 Investigation of water state in PAM-LiCl
- S2.13 MD Simulations of PAM-LiCl and LiCl systems
- S2.14 Desorption performance comparison between PAM-LiCl with other LiCl-based composite sorbents
- S2.15 AWH performance in the homemade device and cycling stability
- S2.16 Quality of collected water
- S2.17 Energy analysis
- S2.18 Cost analysis

S1. Supplementary Methods

S1.1 Chemicals and materials

Chemicals including acrylamide, *N,N*-tetramethylethylenediamine, *N,N'*-methylenebis(acrylamide) (BIS), ammonium persulfate, lithium chloride, polyacrylamide (PAM, $M_w \sim 10,000$, 50 wt% aqueous solution), and poly(acrylic acid) (PAA, $M_w \sim 10,000$, 45 wt% aqueous solution) were purchased from Sigma-Aldrich. Polyvinyl alcohol (PVA, $M_w \sim 15,000$) was purchased from Electron Microscopy Sciences. All the chemicals were used as purchased without further purification.

S1.2 Synthesis and Fabrication

Fabrication of PAM-LiCl gel: In a typical synthesis, acrylamide (AM) precursor solution was prepared by adding 350 mg AM, 30 mg *N,N'*-methylenebis(acrylamide) (BIS), and 10 μl *N,N*-tetramethylethylenediamine (TMEDA) into 10 ml deionized (DI) water. The well-mixed precursor solution was purged with nitrogen for 10 min to remove the dissolved oxygen. Then, 100 μl ammonium persulfate (APS) solution (20 mg/ml) was added into 1 ml precursor solution and mixed by ultrasonic in an ice bath, followed by standing for 3 hours to complete the gelation. The obtained PAM hydrogel was washed by DI water five times to obtain the pure hydrogel with solid content of ca. 5wt%. The purified hydrogel was then immersed into a 10 ml 2.5 wt% LiCl solution overnight to load Li^+ to obtain PAM-LiCl-1; 10 ml 5 wt% LiCl solution was used to load Li^+ for PAM-LiCl-2; 10 ml 10 wt% LiCl solution was used to load Li^+ for PAM-LiCl-3; 10 ml 30 wt% LiCl solution was used to load Li^+ for PAM-LiCl-4. The PAM-LiCl was freeze-dried for 24 hours, followed by an overnight drying at 90°C vacuum oven to fully remove the water residue. Freeze-

drying was performed in a freeze dryer (Labconco, FreeZone 4.5 liter -50C) with the temperature of -50°C and chamber pressure of 0.055 mbar. Finally, the PAM-LiCl gel was ground into fine powder using pestle and mortar for testing.

Fabrication of polymer-LiCl composites: uncrosslinked PAM-LiCl (ucPAM-LiCl), PVA-Li (ucPVA-LiCl) and PAA-Li (ucPAA-LiCl) were fabricated by first preparing a 5 wt% polymer solution. Next, LiCl was dissolved into the polymer solution at 10 wt%. The mixed solution was poured into a petri dish and dried in a 60°C oven overnight. After being further dried in a 90°C vacuum oven for 12 hours, the sample was ready for testing.

S1.3 Characterizations

Dynamic vapor sorption (DVS Adventure, Surface Measurement Systems Ltd.) was used to measure the water sorption performances of sorbents. X-ray diffraction (XRD) patterns were collected by an X-ray Diffractometer (Rigaku, Miniflex 600) with a scanning rate of 10°/min. SEM images were collected by S5500 (Hitachi) to observe the morphology and microstructure of samples. Energy-dispersive X-ray spectroscopy (Bruker EDX system) equipped in the Hitachi SEM was used to obtain the element distribution in the hydrogel. Samples were totally dried and spray-coated with gold (20 mA, 1 min) before the observation. The mechanical properties of gels were tested by rheometer (Discovery HR20, TA Instruments) using a parallel plate on a Peltier plate in the frequency sweep mode at 25°C. Thermogravimetric analyzer (Perkin Elmer, TGA4000) was used to obtain the salt content in gels. The Raman spectrum was measured via spectrometer (WITec alpha300). The excitation radiation for the Raman emission was produced using an Yttrium aluminum garnet laser that had a single-mode operation at 532 nm. The evaporation and

melting behaviors of samples were observed by a differential scanning calorimeter (TA instrument, DSC250) equipped with a refrigerated cooling system (TA instrument, RCS90). Both evaporation and melting curves were tested in nitrogen atmosphere at a flow rate of 50 ml/min, and the ramping rates are 2 K/min and 5 K/min for evaporation and melting, respectively. The concentration of ions was tracked by inductively coupled plasma mass spectrometry (ICP-MS, Agilent 7500ce). A dry cabinet with desiccants inside was used to avoid moisture sorption during transferring the samples for experiments including characterizations and performance measurements.

S1.4 Water collection experiments

The homemade AWH device is composed of a water sorption part and a water collection part. Water sorption part was composed by a humidity generator (based on saturated salt solution), a testing chamber, and a hygrometer. Supersaturated salt solutions are applied to generate moist airflows with controlled RHs by supplying dry airflow into solutions. LiCl solutions coupled with different airflow rates were used to control the humidity in the water sorption chamber to a low RH range. The water collection system is composed of a water collection chamber, a thermometer, and three power sources. Samples are attached to a flexible heating plate in the water collection system, of which the temperature can be controlled by the power source. The weight of PAM-LiCl samples for water collection measurement is ca. 0.25 g. The top condenser wall is tilted at $\sim 45^\circ$ for fast transport of condensed water droplets downward the water collection channel. Heaters are also attached to other walls to elevate their temperature, assisting water vapor to condense at the cooler surface. Thermocouples are connected to the backside of heating plates and condenser surface to monitor and control the temperature.

S1.5 Molecular dynamic simulations

The molecular dynamic (MD) simulations on the PAM-LiCl and LiCl systems at different water concentrations (i.e., water content) were conducted to understand how the water structures in the materials. All simulations were conducted using the LAMMPS software.^[1] The General Amber Force Field (GAFF) was used to model the polymers using the partial charges derived in Rukmani et al.^[2,3] The Joung-Cheatham parameters were used to model lithium chloride ions as this allows for good parametrization of LiCl structure from concentrated to hydrated state.^[4,5] The TIP4P-Ew force field was used to model water due to its compatibility with both the chosen ion force field and long range coulombic solvers, which will be important in the PAM-LiCl simulations.^[6] The water molecules are assumed to be rigid and modeled by using the SHAKE algorithm.^[7] Lorentz-Berthelot mixing rules are used for Lennard-Jones interactions between dissimilar atomic species with $\epsilon_{ij} = \sqrt{\epsilon_{ii}\epsilon_{jj}}$ and $\sigma_{ij} = \frac{\sigma_{ii} + \sigma_{jj}}{2}$. The non-bonded interactions had a cut-off length of 1.2 nm. Long-range coulombic interactions were treated in k-space using the PPPM algorithm.

The total potential energy of the system is given by

$$E = E_b + E_a + E_d + E_{nb}$$

Where

$$E_b = \sum_{bonds} k_b (r - r_{eq})^2$$

$$E_a = \sum_{angles} k_a (\theta - \theta_{eq})^2$$

$$E_d = \sum_{dihedrals} K [1 + \cos(n\phi - \gamma)]$$

$$E_{nb} = \sum_{i,j} \frac{Cq_i q_j}{r} + 4\epsilon_{ij} \left[\left(\frac{\sigma_{ij}}{r_{ij}} \right)^{12} - \left(\frac{\sigma_{ij}}{r_{ij}} \right)^6 \right]$$

k_b , k_a , and K are force constants. r_{eq} and θ_{eq} are equilibrium positions. E_b , E_a , and E_d are bonded interactions. E_{nb} are nonbonded interactions including coulombic and Lennard-Jones interactions.

To prepare the initial conditions of the simulations, Moltemplate was used to generate the input files.^[8] Four straight PAM chains with a degree of polymerization of 40 were randomly inserted into a simulation box with side lengths of 90 Angstroms using Packmol.^[9] A short steepest descent minimization was conducted to remove local high energy configurations. The simulation box was then compressed using a constant engineering strain rate of -0.01/ps at 1500 K to generate random chain configurations at different volumes. Snapshots of the chain configurations were output to be within 10% of the equilibrium volume of water and v at ambient conditions. The chain coordinates were inputted into Packmol, and water molecules and salt ions were randomly inserted into the simulation box. The ratio of LiCl ions to PAM monomers was set at 3.56 to match experimental conditions. A short steepest descent was conducted to remove local high energy configurations. The system was subsequently equilibrated at 600 K in the NVT ensemble for 100 ps and in the NPT ensemble at 600 K and 1 atm for 10 ns to promote polymer and ion diffusion. The system was then cooled to 298 K at a ramp rate of 20 K/ns. An NPT equilibration at 298 K and 1 atm was conducted for 5 ns to equilibrate the system density. The last 1 ns of this equilibration step was used to calculate the system average density. Using the average density calculated in 3 independent runs, the volume of each independent run was adjusted using a constant engineering strain rate over 1 ns and equilibrated at constant NVT for an additional 1 ns. Finally, a 2 ns production run was conducted to calculate the system properties.

To prepare the initial conditions for LiCl solution simulations, ions and water molecules were randomly inserted using Packmol to achieve density within 10% of the equilibrium value. A short

steepest descent minimization and NVT equilibration at 298 K were conducted for 100 ps followed by an equilibration in the NPT ensemble for 5 ns. The last 1 ns of this equilibration step was used to calculate the system density.

For both the PAM-LiCl and LiCl simulations, all equilibration steps used the Langevin thermostat with a damping constant of 100 ps and the Berendsen barostat with a damping constant of 1000 ps.^[10,11] The production runs used the Nosé-Hoover thermostat with a damping constant of 100 ps.^[12,13] The timestep interval was chosen to be 1 fs. The radial distribution functions were outputted every 10 ps and snapshots of the trajectory were outputted every 50 ps for hydrogen bond analysis.

The hydrogen bonding structures were calculated using geometric criteria between the acceptor, donor, and hydrogen atoms.

$$HB = \begin{cases} 1, & |\vec{r}_a - \vec{r}_d| < r_{min} \text{ and } \theta_{adh} < 30^\circ \\ 0, & \text{otherwise} \end{cases}$$

Where r_{min} is the cutoff distance between the acceptor and donor atoms. The cutoff distances used were based on the distance of the first trough in RDF curves in the 3.5 g/g water content simulations. Defined acceptor atoms are $O_{Polymer}$, $N_{Polymer}$, O_{Water} , and Cl. Defined donor atoms are $N_{Polymer}$ and O_{Water} . The angle cutoff between the acceptor, donor, and hydrogen atom was 30° , which is a common cutoff used in hydrogen bond calculations.^[14-16] Due to the strong interactions between water and lithium ions even without formation of hydrogen bonds, the first coordination number of water around lithium ions was also calculated. The cutoff distance for the first coordination shell is equal to the minimum of first trough in the RDF curve. The proportion of hydrogen bond sites occupied by each adsorbent group and water is defined below.

$$Fraction\ of\ n_{HB} = \frac{n_{HB}}{4 * n_w}$$

Where n_{HB} is the number of hydrogen bonds and n_w is the number of water molecules in the simulation.

S2. Supplementary Figures

S2.1 Microscopic observation of PAM-LiCl

SEM image in Figure S1 shows the micro-size particles of PAM-LiCl. After ground into powder, PAM-LiCl showed the size between 2 and 25 μm , exposing more active sites that promoted the sorption kinetics. During desorption, the large surface area also helps the fast water release.

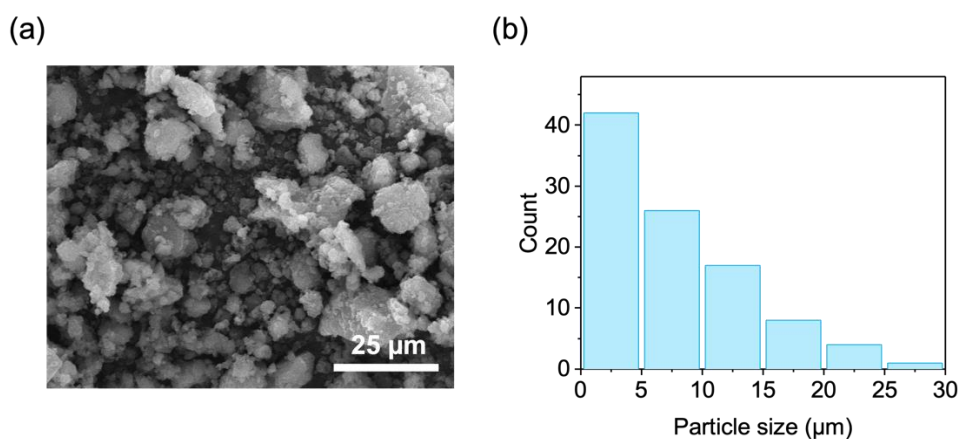


Figure S1. (a) SEM image of PAM-LiCl. (b) Distribution of particle size of PAM-LiCl.

Since LiCl solution is evenly dispersed in the PAM hydrogel matrix during loading and we adopted a very gentle freeze-drying method to obtain the final PAM-LiCl gel, the salt distribution will not be affected by the drying process and maintain the uniform state, which is proven by EDX mapping results (Figure S2).

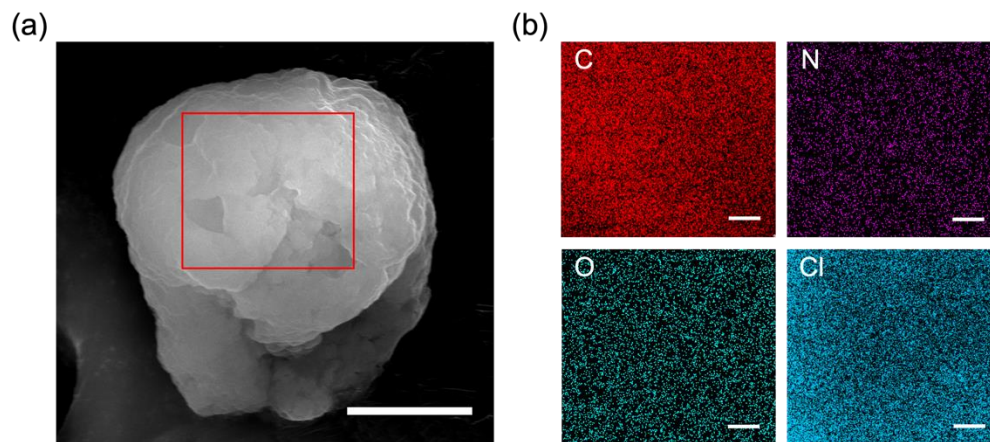


Figure S2. (a) SEM image and (b) EDX mapping images of PAM-LiCl. The red rectangle in (a) is the EDX mapping region. Scale bar: (a) 5 μ m; (b) 1 μ m.

S2.2 Mechanical property of PAM-LiCl and PAM gel

The mechanical property of PAM-LiCl gel and PAM hydrogel were characterized via testing its storage modulus (G') and loss modulus (G'') values. The G' and G'' values of pure PAM hydrogel and PAM-LiCl at water content of 1 g/g are shown in Figure S3. For PAM hydrogel, G' is an order of magnitude higher than G'' throughout the entire frequency range, indicating the predominance of elastic property over viscous behavior. And the hardly changed slopes of G' and G'' curves represent the characters of the gel state. PAM-LiCl showed almost similar G' and G'' values with those of pure PAM hydrogel, which is attributed to the similar skeleton structure brought by the crosslinked PAM network. These results confirmed the hydrogel state of the PAM-LiCl.

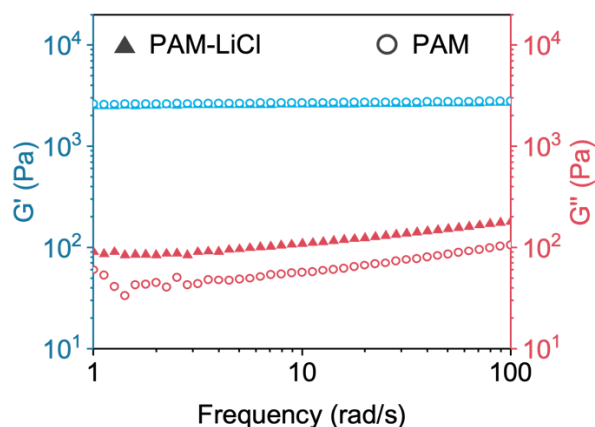


Figure S3. Storage moduli (G') and loss moduli (G'') of PAM-LiCl and PAM hydrogel at water content of 1 g/g.

S2.3 Water sorption behaviors of uncrosslinked PAM-LiCl, PVA-LiCl and PAA-LiCl

Water sorption performances of ucPAM-LiCl, ucPVA-LiCl and PAA-LiCl were characterized using DVS at 20%RH, 25 °C. Uncrosslinked polymer-Li composites were used to eliminate the potential effects of crosslinking density difference to solely reflect polymer functional groups' influence on equilibrium water uptake. LiCl content in each polymer-Li composite is the same (~67 wt%). As shown in Figure S4a, ucPAM-LiCl showed higher water uptake than ucPVA-LiCl and ucPAA-LiCl from 20%RH to 60%RH. When testing the sorption tests at 20%RH, it can be seen that ucPAM-LiCl outperformed the others regarding both sorption kinetics and water uptake. The high performance of ucPAM-Li can be attributed to the high hydrophilicity of the amide groups.

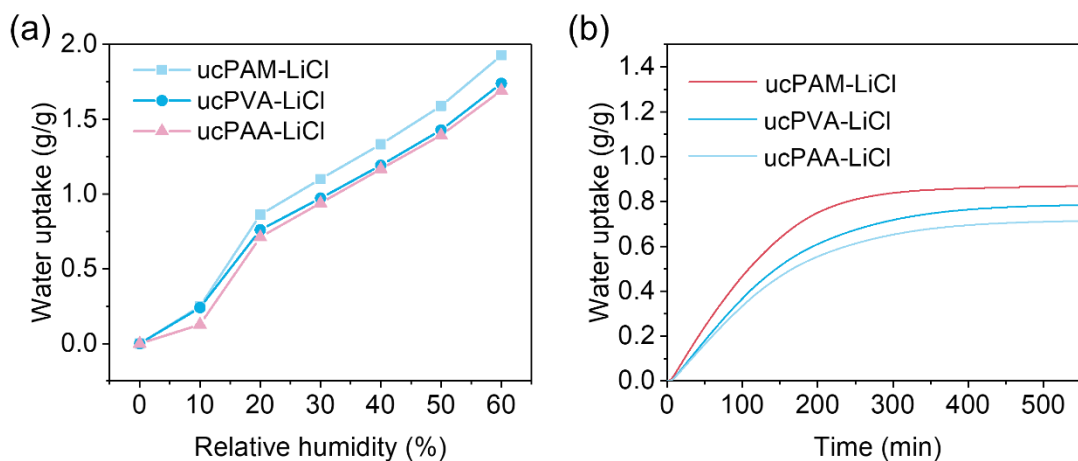


Figure S4. (a) Sorption isotherms of ucPAM-LiCl, ucPVA-LiCl, and ucPAA-LiCl. (b) Sorption performance of ucPAM-LiCl, ucPVA-LiCl and ucPAA-LiCl at 20%RH, 25 °C.

S2.4 Optimizing the Li content in PAM-LiCl

To investigate the effect of LiCl content on sorption performance and heat of desorption, PAM-LiCls with different LiCl content were prepared and named as PAM-LiCl-1, PAM-LiCl-2, PAM-LiCl-3, and PAM-LiCl-4. TGA was conducted to obtain the LiCl content in each gel sample. As shown in Figure S5a, the results show that LiCl contents increased from PAM-LiCl-1 to PAM-LiCl-4, which are ca. 40 wt%, 56 wt%, 68 wt%, and 78 wt%, respectively. Sorption performance tests of these samples were performed under 20%RH, 25 °C by DVS. As shown from Figure S5b, as LiCl content increased from 40 to 68 wt% (PAM-LiCl-1 to PAM-LiCl-3), both equilibrium water uptake and sorption kinetics increased owing to enhanced hygroscopicity in PAM-LiCls brought by the higher LiCl amount. When LiCl concentration further increased to 78wt%, the obtained PAM-LiCl-4 showed higher water uptake but lower sorption kinetics than PAM-LiCl-3, implying the optimized LiCl content is 68 wt%. The possible reason for this phenomenon is that too much LiCl will induce aggregation, impeding the exposure of active sites and leading to a

reduced contact area with air, thus causing a lowered sorption kinetics. Therefore, PAM-LiCl-3 was chosen to be the target sample for the following experiments.

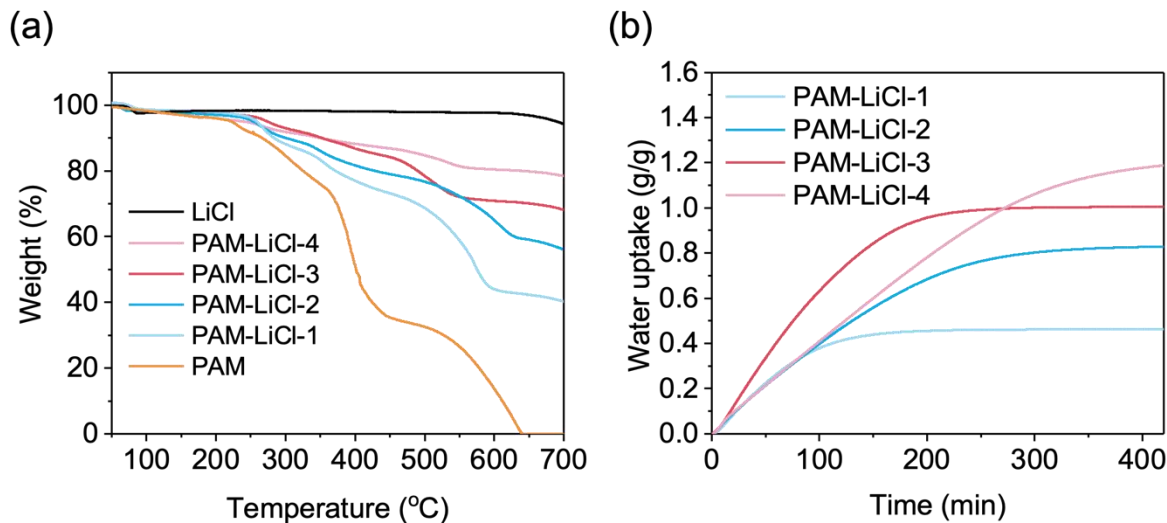


Figure S5. (a) TGA curves of LiCl, PAM-LiCl-1, PAM-LiCl-2, PAM-LiCl-3, PAM-LiCl-4, and pure PAM in air atmosphere. (b) Sorption properties of PAM-LiCl-1, PAM-LiCl-2, PAM-LiCl-3, and PAM-LiCl-4 at 20%RH, 25 °C by DVS.

S2.5 Water sorption isotherm of PAM

Figure S6 shows the isotherm of pure PAM gel from 0%RH to 90%RH at 25°C. The PAM had poor water sorption capacity due to lack of hygroscopic sites. It didn't reach above 0.1 g/g water uptake until RH > 50%. Although the water uptake of PAM had a larger increase in the high RH region, its overall water uptake performance is much poorer than PAM-LiCl.

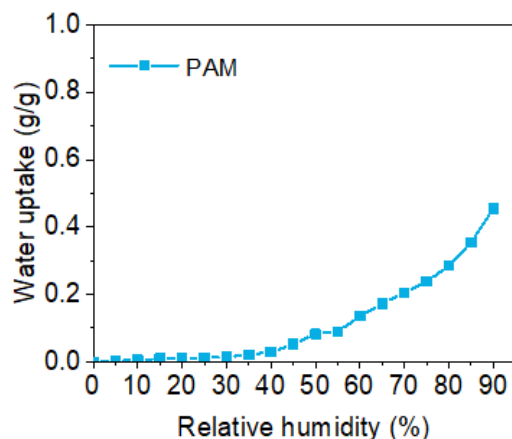


Figure S6. Isotherm of PAM gel at 25 °C.

S2.6 Sorption performance comparison between PAM-LiCl and literature

We summarized the water uptake performance at low RH conditions of other reported sorbents in literature in Table S1. Compared to previously reported sorbents, PAM-LiCl showed a higher water uptake at both 20% RH and 30% RH. As for water sorption kinetics, we estimated the sorption rate (g/g/min) by dividing water uptake (g/g) by the minimum time required for reaching 90% of the equilibrium water uptake. As can be seen from Table S1, PAM-LiCl showed the fastest sorption rate of 0.0080 g/g/min among other sorbents. Altogether, PAM-LiCl showed its competitiveness as an effective sorbent in arid regions.

Table S1. Summary of water sorption performance of reported salt-based sorbents in various types.

Type	Materials	Temperature (°C)	RH (%)	Water uptake (g/g)	Time for reaching 90% water uptake (min)	Sorption rate (g/g/min)	Reference
Salt-based composites	PAM-LiCl	25	20	1.1	~138	0.0080	This work
			30	~1.5	~92	0.0163	

HCS-LiCl	25	15	~0.4	~600	0.0007	[17]	
		35	~0.7	~200	0.0035		
ACFF-Silica sol-LiCl 30	25	20	~0.4	/	/	[18]	
		30	~0.5	/	/		
P-C-MgCl ₂ (Alginate- MgCl ₂)	30	20	~0.4	/	/	[19]	
		30	~0.9	/	/		
Active Carbon Felt- LiCl	25	20	~0.5	/	/	[20]	
		30	~0.8	/	/		
PAM-CNT- CaCl ₂	25	35	~0.7	~500	0.0014	[21]	
MIL-101(Cr)- CaCl ₂	30	30	~0.8	/	/	[22]	
LiCl@MIL- 101(Cr)_51	30	20	~0.6	/	/	[23]	
		30	~0.8	~150	0.0053		
C-CaCl ₂ (Alginate- CaCl ₂)	30	20	~0.6	/	/	[19]	
		30	~0.9	/	/		
Alginate- CaCl ₂	28	20	~0.7	/	/	[24]	
		25	~0.8	~360	0.0022		
		30	~1.0	/	/		
LiCl@rGO- SA	30	15	~1.0	~160	0.0063	[25]	
		30	~1.5	~120	0.0125		
MIL-160	30	20	~0.35	/	/	[26]	
		30	~0.36	/	/		
MOF-333	25	20	~0.39	/	/	[27]	
		30	~0.40	/	/		
MOF-801-P	25	20	~0.28	/	/	[28]	
		30	~0.31	/	/		
Co ₂ Cl ₂ BTDD	25	20	~0.2	/	/	[29]	
		30	~0.8	/	/		
Carbon- based composites	Steam-80	25	20	~0.1	~30	0.0040	[30]
		30	~0.2	~40	0.0043		
Gel-based composites	PAETA-Ac	25	20	~0.24	/	/	[31]
		30	~0.30	/	/		
	PCD-MOF gel	25	30	~0.6	~1200	0.0004	[32]

S2.7 Salt leakage prevention effects of PAM-LiCl

The hydrogel network of PAM-LiCl served as a water reservoir that can not only store the absorbed water but also prevent salt leakage, avoiding the potential corrosion issues during application. To

confirm the salt leakage prevention effect of PAM-LiCl, we put the gel on a Kimtech paper before and after moisture sorption to see if any water could be extracted from the swollen PAM-LiCl. Figure S7a shows no salt can be observed when putting the dry PAM-LiCl on the Kimtech wipe. After absorbing moisture at ~60%RH, the PAM-LiCl with a water uptake of 2.5 g/g also showed almost no liquid leaking out (Figure S7b). These results show that the PAM-LiCl can prevent LiCl leakage during water capturing, which is a desired property for actual applications.

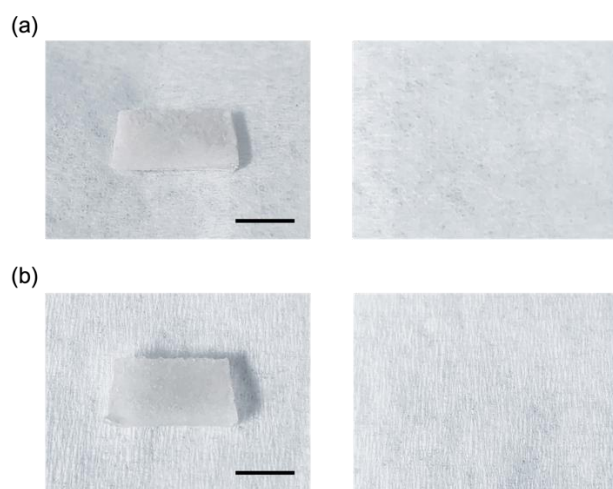


Figure S7. Photos showing PAM-LiCl can prevent the LiCl from leaking. (a) Dry PAM-LiCl (left) and the wipe underneath (right). (b) Wet PAM-LiCl (left) after sorption and the wipe underneath (right). Scale bar: 1cm.

S2.8 Water sorption and desorption rate of PAM-LiCl and LiCl

Figure S8 presents the derivative weight change of PAM-LiCl and LiCl during sorption and desorption. Upon exposure to moisture at 20%RH, PAM-LiCl's sorption rate quickly rose and then slowly reduced, while LiCl showed a steadily slow sorption rate. Upon heated to 70°C, PAM-LiCl can desorb water with a large desorption rate up to 0.13%/min. In contrast, LiCl only showed a desorption rate of 0.04%/min first 10 minutes and then slowed to a low rate of ~0.003%/min.

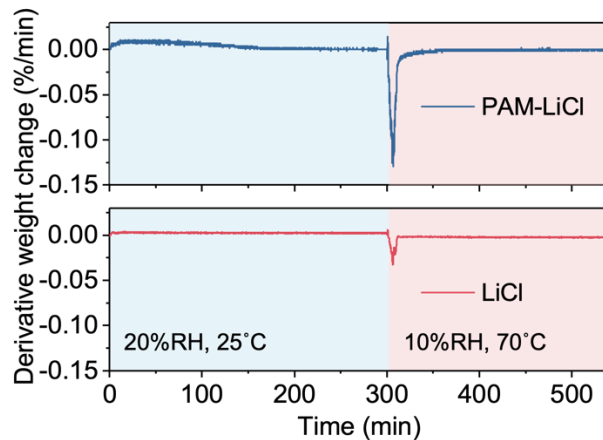


Figure S8. Derivative weight change of PAM-LiCl, LiCl showing the sorption and desorption rates.

To investigate the effects of specific surface area on the sorption and desorption rates, we prepared a monolithic bulk PAM-LiCl as a control sample to compare with PAM-LiCl microgel. Thickness of the monolithic PAM-LiCl is $\sim 800\mu\text{m}$, and the average size of the PAM-LiCl microgel is $\sim 10\mu\text{m}$. As shown in Figure S9, the monolithic sample has a lower sorption rate (3.1 mg/g/min) than that of microgel sample (7.6 mg/g/min). Similarly, the monolithic sample also has a lower desorption rate of 2.6 mg/g/min than the microgel sample (37 mg/g/min). These results indicate that a higher specific surface area will lead to a high sorption/desorption rate. In addition, under the same conditions, the powder LiCl showed the lowest sorption and desorption rates (2.6 mg/g/min and 2.1 mg/g/min) confirming the validity of our material design (Figure 2b).

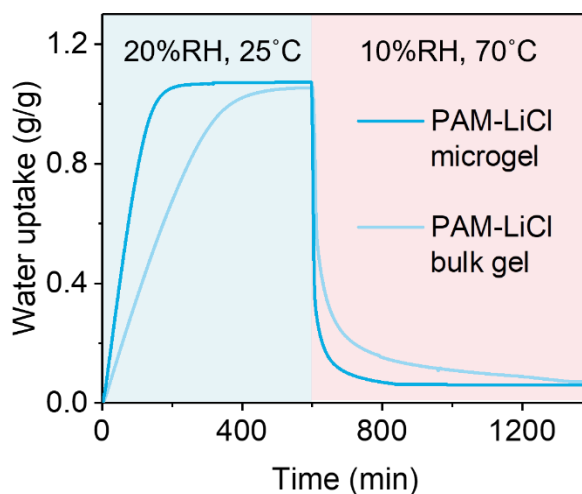


Figure S9. Water sorption and desorption kinetics of powder and monolithic PAM-LiCl and powder PAM-LiCl. Sorption condition: 20%RH, 25 °C; desorption condition: 10%RH, 70 °C.

S2.9 Desorption heat PAM-LiCl and LiCl

We have proven in Figure 3 that PAM-LiCl showed a reduction in desorption heat compared to LiCl at the same water content ($H_2O/sorbent$ ratio). The $H_2O/LiCl$ ratio in LiCl and PAM-LiCl is different at the same $H_2O/sorbent$, which could lead to a change in desorption heat. Therefore, we measured the desorption heat of PAM-LiCl and LiCl at the same $H_2O/LiCl$ ratios to decouple the effect of the $H_2O/LiCl$ ratio. As shown in Figure S10, PAM-LiCl with $H_2O/LiCl$ content of 0.5, 1, and 1.5 g/g showed desorption heat of 3372 J/g, 2725 J/g, and 2608 J/g, respectively; LiCl with $H_2O/LiCl$ ratio of 0.5, 1, and 1.5 g/g shows desorption heat of 3511 J/g, 2934 J/g, and 2734 J/g, respectively. As a result, PAM-LiCl shows lower desorption heat than LiCl, with an average difference in desorption heat of ca. 200 J/g. As shown in Figure 3b, the average reduction in desorption heat of PAM-LiCl compared to LiCl is ca. 300 J/g at the same $H_2O/sorbent$ ratio. These results reveal that the polymer-water interaction contributes to ~67% of the desorption heat

difference between PAM-LiCl and LiCl, thereby being the primary reason for the lower desorption heat.

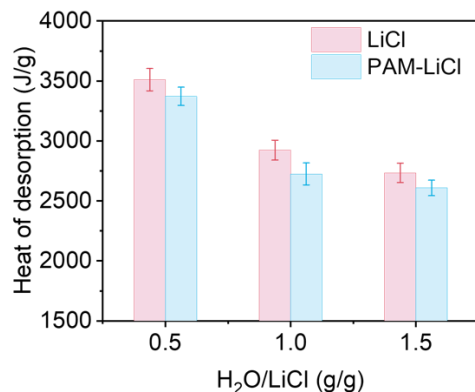


Figure S10. The heat of desorption of LiCl and PAM-LiCl at water-to-LiCl (H₂O/LiCl) ratio of 0.5, 1.0, and 1.5g/g.

S2.10 Freezable water content in PAM-LiCl and LiCl

DSC melting tests were conducted to characterize the freezable water content in PAM and LiCl at different water contents. During the DSC measurements, the samples were heated from -90 to 20 °C with a heating rate of 5 °C/min under nitrogen flow flux (50 mL/min). Figure S11 shows the heat flow curves along with temperature change of PAM-LiCl and LiCl. As water content changed from 2 to 5 g/g, vshowed an increased melting peak area as well as the higher melting peak temperature. In contrast, LiCl didn't show a melting peak until water content reached 4 g/g. To estimate the freezable water content, heat of fusion was first calculated based the on the following equation:^[33]

$$\Delta H(T) = \Delta H(273) - \int_T^{273} \Delta C_p dT$$

Where $\Delta H(273)$ is the melting enthalpy of normal water and ΔC_p is the difference of heat capacity between supercooled water and ice. This $\Delta H(T)$ (J/g) is approximately expressed as the equation:

$$\Delta H(T) = \Delta H(273) + 2.119 \cdot \Delta T - 0.00783 \cdot \Delta T^2$$

Where ΔT is the temperature difference between melting temperature of supercooled water (T) and freezing point of normal water ($0\text{ }^\circ\text{C}$). Therefore, the freezable water content (Q_f , g/g) in PAM-LiCl and LiCl can be estimated by the following equation:

$$Q_f = \frac{\Delta Q}{\Delta H(T) \cdot W_d}$$

Where W_d (g) is the weight of dry sample, and ΔQ (J) is the heat of freezable water calculated from the DSC measurement.

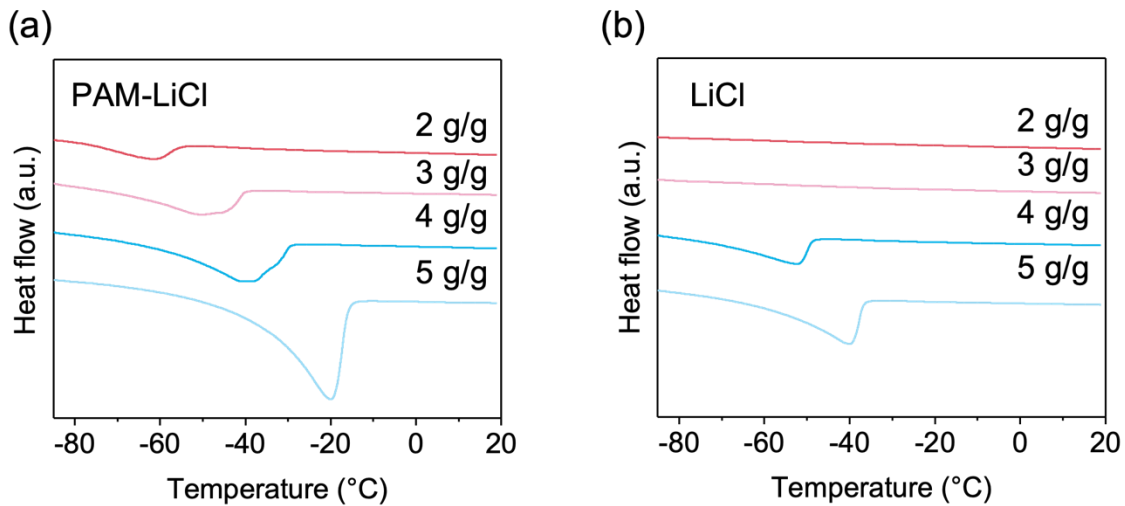


Figure S11. DSC heat flow curves during melting of (a) PAM-LiCl and (b) LiCl at water content of 2 g/g, 3 g/g, 4 g/g and 5 g/g.

The calculated freezable water contents are summarized in Table S2. At the same water content, PAM-LiCl showed higher freezable water content than LiCl, proving that PAM network can enable more freezable water which will be easier to evaporate. A higher freezable water content will lead to a lower heat of desorption and promote the water release process.

Table S2. Heat of fusion and freezable water content of PAM-Li and LiCl.

Water content (g/g)	PAM-LiCl		LiCl	
	Heat of fusion (J/g)	Freezable water content (g/g)	Heat of fusion (J/g)	Freezable water content (g/g)
2	42	0.46	0	0
3	46	0.60	0	0
4	67	1.10	33	0.63
5	112	2.02	63	1.34

S2.11 Evaluation of heat of sorption of PAM-LiCl

The heat of sorption of PAM-LiCl was obtained by first measuring the sorption isotherms at different temperatures (Figure S12a). Then, the corresponding equilibrium pressures P at different temperatures T were obtained and the $\ln P$ vs. $1/T$ diagram was plotted (Figure S12b). According to the Clausius-Clapeyron equation, we can obtain the heat of sorption ΔH_{sorp} , whose value is the slope of the curve of $\ln P$ vs. $1/T$ multiplied by gas constant R.^[27]

$$\ln \frac{P_1}{P_2} = -\frac{\Delta H_{sorp}}{R} \cdot \left(\frac{1}{T_1} - \frac{1}{T_2} \right)$$

The obtained values of ΔH_{sorp} varying with water uptake is shown in Figure S12c.

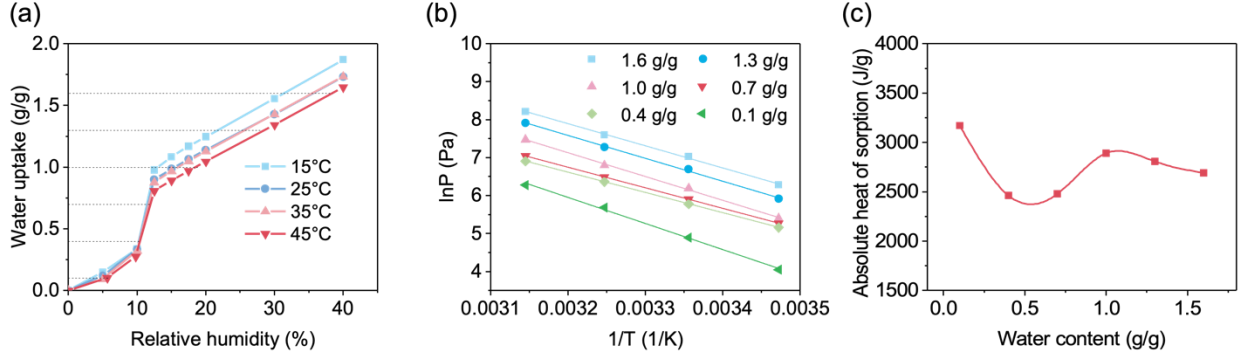


Figure S12. (a) Isotherm curves of PAM-LiCl at 15°C, 25°C, 35°C and 45°C. (b) ln (P) vs. 1/T curves. (c) Heat of sorption of PAM-LiCl at different water contents.

S2.12 Investigation of water state in PAM-LiCl

It has been proven in previous studies that liquid water molecules exist in different configurations as the types of hydrogen bonds vary. The basic hydrogen bond structure is tetrahedral and non-tetrahedral. In hydrogel, the hydrophilic groups participating in hydrogen bonding with water thus would change the hydrogen bond environments around water molecules.^[34] Raman spectra were sensitive to the hydrogen-bonding configuration of the water molecules, and is able to show scattering peaks from O-H assigned into two types of water: (1) water molecules with four hydrogen bonds paired from two protons and two lone electron pairs, which refers to free water; (2) weakly or non-hydrogen bonded water molecules where the hydrogen bonds are partially or totally broken.^[34] The weakly or non-hydrogen bonded water corresponds to the intermediate water in hydrogel. As shown in Figure S13, the Raman spectra of PAM-LiCl after sorption with a

water content of 1 g/g showed a small peak corresponding to C-H at around 2900 cm^{-1} and a broad peak related to O-H at around 3450 cm^{-1} , which was fitted into five peaks. Peaks at 3078 , 3238 , 3412 cm^{-1} are assigned to free water which are shown as blue curves, and the red curves with peaks at 3515 and 3627 cm^{-1} correspond to the intermediate water. The result confirms the existence of the intermediate water in PAM-LiCl, which will facilitate the water desorption.

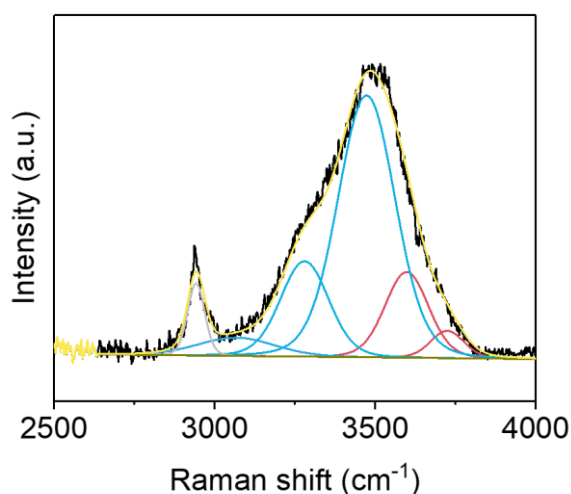


Figure S13. Raman spectra of PAM-LiCl with water uptake of 1 g/g.

S2.13 MD Simulations of PAM-LiCl and LiCl systems

We assessed the NPT equilibration of the simulations by tracking the fluctuations in density. Figure S14 shows the fluctuations in the simulation cell density during NPT equilibration for PAM-LiCl at a water content of 2.5 g/g. It can be seen that all three runs had similar densities fluctuating about an equilibrium value. The dotted line shows the running average density of all three simulation runs for the final nanosecond of equilibration to be used as an input in the NVT production run.

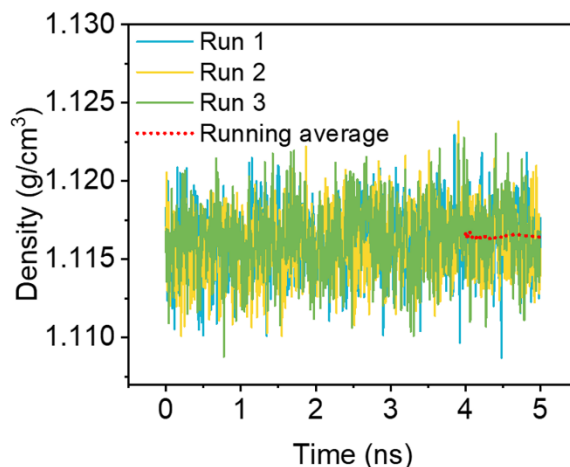


Figure S14. Density fluctuations of three independent runs for NPT equilibration of PAM-LiCl at a water content of 2.5 g/g. Each of the solid lines represents an independent run and the dotted line shows the running average density.

The angle formed between the dipole vector of the water molecule and the vector separating the oxygen atom and ion are calculated to characterize the type of bonding formed between water and ions as a function of water content in Figure S15. It can be seen that the probability distribution function (PDF) of bond angles made by each water molecule and neighboring lithium ions narrows slightly with increasing water content with a peak at 160 degrees. This suggests that water tends to form an intermediary structure between a tetrahedral angle and an aligned dipolar angle with the ions. In contrast, the PDF of water's dipolar angles around chlorine ions shows much larger changes as a function of water content. The largest peak at about 53 degrees more than doubles from 0.03 to 0.07, which is close to the ideal tetrahedral angle formed by water's hydrogen bonding network. A second peak at around 136 degrees decreases and flattens out with increasing water content. This secondary peak comes from the adjacent water molecules tightly bound to a neighboring lithium ion.

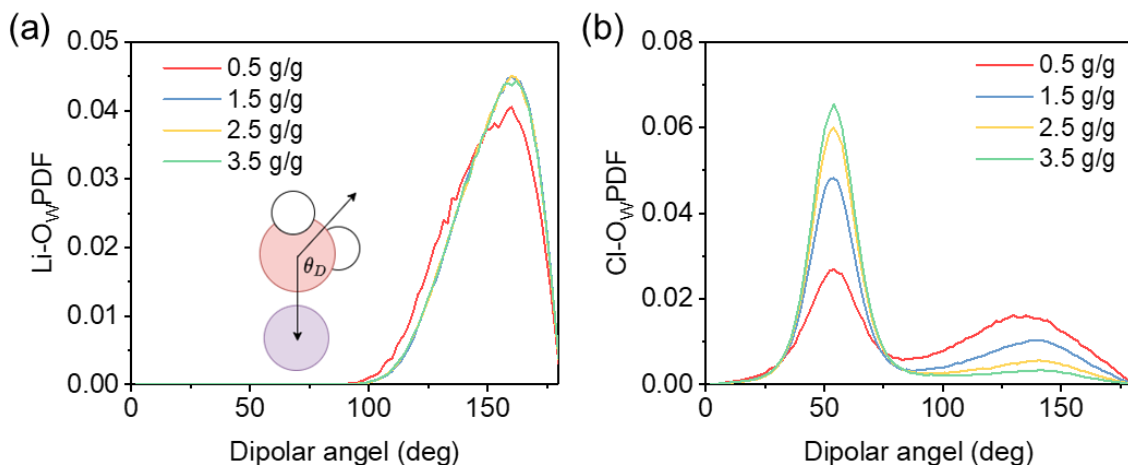


Figure S15. Probability distribution of angle formed between dipolar vector and (a) lithium ion or (b) chlorine ion for PAM-LiCl simulations with water contents of 0.5, 1.5, 2.5, and 3.5 g/g.

The radial distribution functions (RDF) of water's oxygen atom around ions are plotted in Figure S16. Plotting the RDF of water around lithium ions reveals that water is highly structured in the first coordination shell, with the first peak and first trough occurring at the same distances for both low and high water contents. In contrast, it can be seen that the RDF curve for water around chlorine ions changes with the increase of the water content. At a water content of 0.5 g/g-PAM-LiCl, the first peak is broad and occurs at about 3.5 Å and first trough at 4.23 Å. Once the water content increases to 3.5 g/g-PAM-LiCl, the first peak becomes much narrower. Both the peak and the trough also shift to smaller values of 3.12 and 3.89 Å, respectively. These changes in the RDF curves suggest that water first structures itself around lithium ions at low water contents and then around chlorine ions.

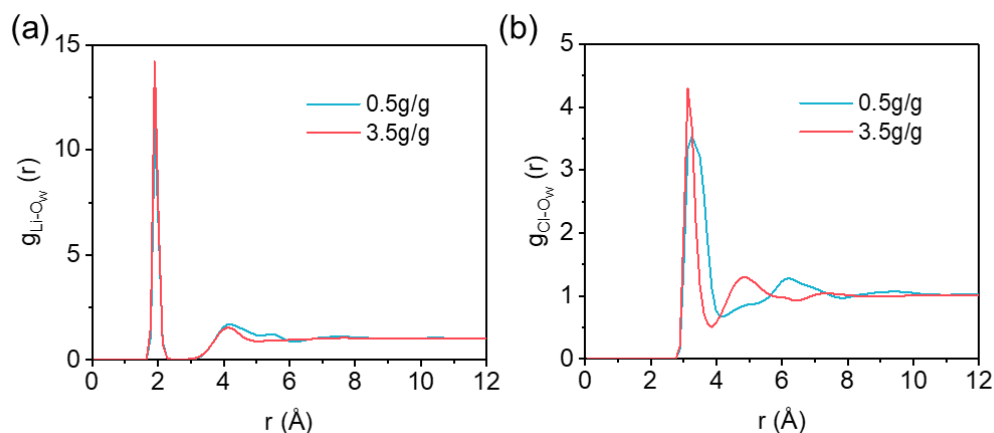


Figure S16. Radial distribution functions of water's oxygen atom around (a) lithium ions and (b) chlorine ions for 0.5 and 3.5 g-H₂O/g-PAM-LiCl simulations.

The radial distribution functions for water and the different hydrogen bonding atoms in the polyacrylamide chain were also calculated for low and high water content in Figure S17. It can be seen in the left graph that water interacts strongly with the oxygen in the amide functional group, leading to a high peak of about 1.56 at the 0.5 g-H₂O/g-PAM-LiCl. The peak drops to 1.17 when water content is increased to 3.5 g-H₂O/g-PAM-LiCl due to increasing hydration of the system. In contrast, the first peak of water's radial distribution function around nitrogen atoms shows a slight increase from 1.13 to 1.20, suggesting slightly stronger relative interactions with increasing hydration.

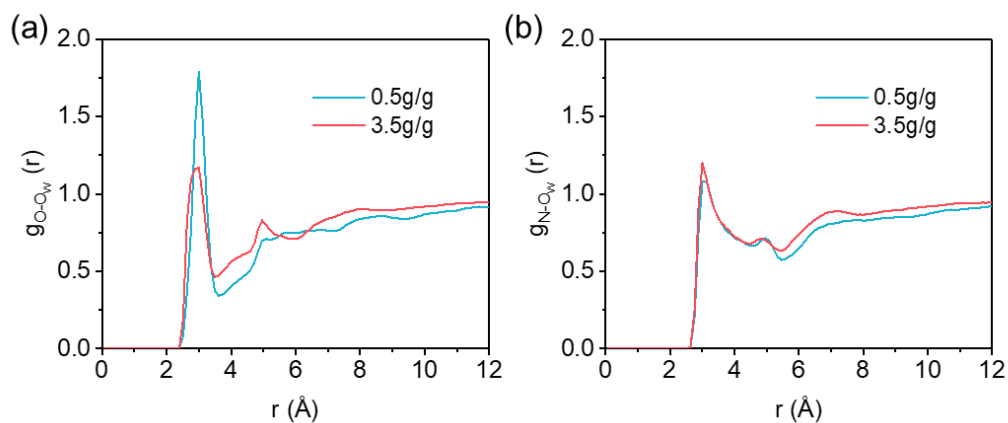


Figure S17. Radial distribution functions of water's oxygen atom around (a) oxygen atoms and (b) nitrogen atoms in polyacrylamide for 0.5 and 3.5 g-H₂O/g-PAM-LiCl simulations.

To calculate the proportion of hydrogen bond sites occupied, we first need to determine the number of hydrogen bonds in the system. Figure S18 shows the average number of hydrogen bonds formed between the polymer-water (P-W) and water-water (W-W) in the PAM-LiCl and LiCl solution simulations normalized to the adsorbent group. For example, the P-W curve in Figure S18a is equal to the total number of hydrogen bonds between polymer and water divided by the total number of acrylamide monomers. It is found that in the studied range, the number of hydrogen bonds increases roughly linearly with water content. The number of hydrogen bonds formed between P-W is slightly larger than W-W inside of the PAM-LiCl simulation, showcasing the hydrophilicity of the polymer used. In contrast, the number of hydrogen bonds formed with chlorine ions and the number of water molecules in the first solvation shell of lithium increases rapidly at low water contents and then saturates at high water contents as seen in S18b. This is because the high hydrophilicity of the ions causes water to first adsorb around the salt and leads to a faster rate of occupancy inside of the ions' first solvation shell. It can also be seen that the number

of interactions in the LiCl solution is systematically lower than the corresponding number in the PAM-LiCl simulation, although the difference decreases with increasing water content.

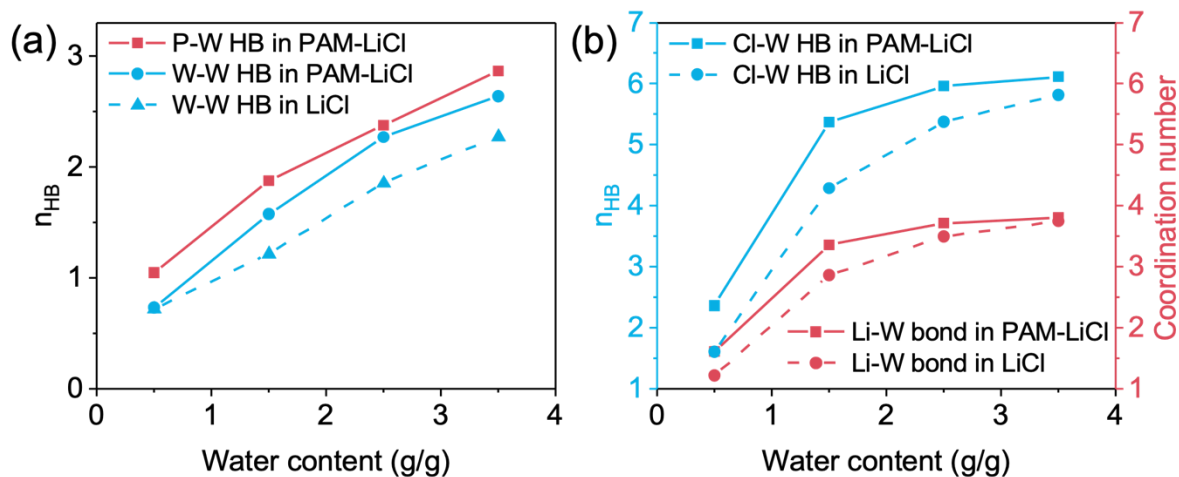


Figure S18. (a) Total number of hydrogen bonds formed between polymer and water (P-W HB) per monomer and between water and water (W-W HB) per water molecule in the PAM-LiCl and LiCl simulation. (b) Total number of hydrogen bonds formed between chlorine and water (Cl-W HB) per chlorine ion and coordination number of water around lithium (Li-W bond) in the PAM-LiCl and LiCl simulation.

It was found that all ensemble averaged Mean Squared Displacement (MSD) graphs showed linear behavior beyond the 200 ps mark by plotting it on a log-log graph. As a result, the diffusivities were calculated by fitted a linear line to the curves from the 200 ps to the 2 ns region as seen in Figure S19. The diffusion coefficients is then given by the slope in the linear regime.

$$D = \frac{1}{6} \frac{d}{dt} MSD$$

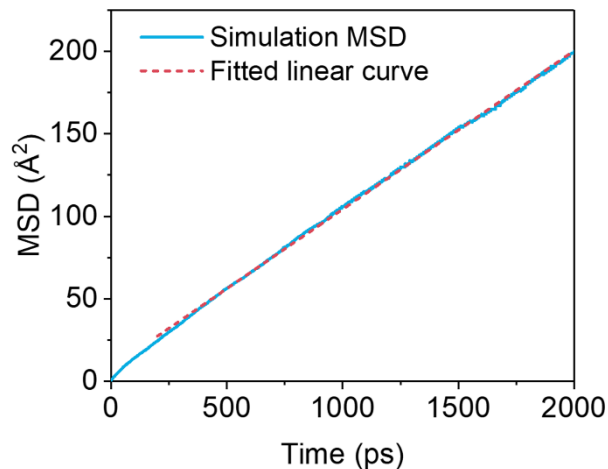


Figure S19. Ensemble average mean squared displacement of water molecules in the 1.5 g-H₂O/g-PAM-LiCl simulations on a linear graph with the fitted line between 200 ps and 2 ns time domain.

The distribution of final MSDs in each system are plotted using both a probability distribution and a cumulative distribution representation in Figure S20. 500 evenly spaced bins are used from 0 to the maximum MSD at each water content. It can be seen that the LiCl solution has a higher and narrower peak in the probability distribution than the PAM-LiCl system at the same water content for all values of water content above ~0.5 g/g. This shows that more water molecules are highly immobile and do not diffuse significantly during the simulation time. This behavior is reflected in the cumulative distribution, which is simply the cumulative sum of the probability distribution graph. It can be seen that the cumulative distribution approaches 1 at a faster rate for the LiCl simulation than the PAM-LiCl simulation, showcasing the higher number of immobile water molecules.

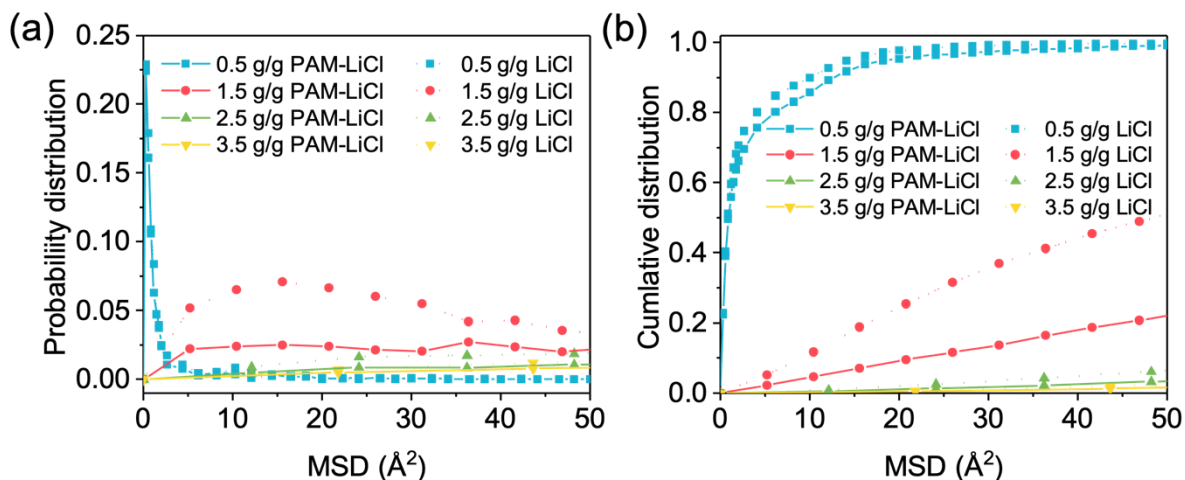


Figure S20. (a) Probability distribution and (b) cumulative distribution of final MSD of water molecules after 2 ns in the PAM-LiCl simulations and LiCl simulations.

S2.14 Desorption performance comparison between PAM-LiCl with other LiCl-based composite sorbents

We assessed the water desorption performance of PAM-LiCl by comparing it with LiCl-based composite sorbents prepared by loading LiCl into different kinds of matrices, such as MOFs,^[35] porous carbon,^[17,18,20] and silica gels (Figure S21).^[36] The corresponding data are also listed in Table S3 along with the desorption conditions. In the water release column of Table S3, water release (g/g) refers to desorbed water (g) divided by dry sorbent weight (g), and the percentage represents the release ratio, equal to the desorbed water (g) divided by absorbed water (g). After moisture sorption at 20% RH, 25 °C, PAM-LiCl delivered a high water release of 1 g/g under 70 °C, with a release ratio of 91%. In comparison, other salt-based sorbents showed lower water release values or release ratios at similar desorption conditions. Additionally, by dividing the water release (g/g) by the minimum time required for reaching 90% of the water release, we obtained the desorption rates for all the listed sorbents, in which PAM-LiCl exhibited highest desorption rate

of 0.037 g/g/min. We further compared PAM-LiCl's desorption behavior with other sorbents including MOFs,^[29] carbon-based,^[30] and gel-based composites.^[31] As can be seen in Table S3, PAM-LiCl shows higher water release and desorption rate than other sorbents. Both high water release and desorption rate of PAM-LiCl enabled by the PAM matrix make it a suitable sorbent material for AWH in arid conditions.

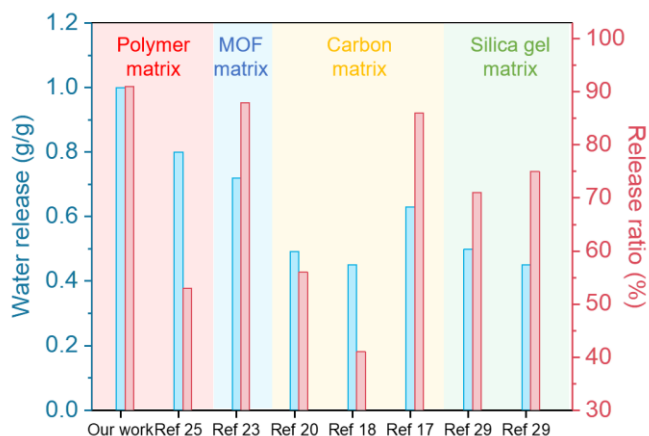


Figure S21. Summary on water desorption performance of salt composites with different matrices. Red, blue, yellow, and green regions refer to polymer matrix; MOF matrix; carbon matrix; and silica gel matrix, respectively.

Table S3. Summary of water desorption performance of reported sorbents in various types.

Type	Materials	Desorption conditions	Water release (g/g)	Release ratio	Time for reaching 90% of total release (min)	Desorption rate (g/g/min)	Reference	
Salt-based composites	Matrix type Polymer	PAM-LiCl	70°C, 10%RH	~1.0	~91%	~27	0.037	This work
		LiCl@rG O-SA	70°C, 14%RH	~0.8	~53%	~60	0.013	[25]
		MOF LiCl@MI L-101(Cr)_51	83°C, 8%RH	~0.6	~86%	~24	0.025	[35]

Carbon	ACF-LiCl	65°C, 14%RH	~0.5	~56%	/	/	[20]
	ACFF- Silica sol- LiCl 30	80°C, /	~0.5	~41%	~130	0.004	[18]
	HCS-LiCl	80°C, /	~0.6	~86%	~50	0.012	[17]
Silica gel	SGA-LiCl	70°C, /	~0.5	~71%	~20	0.025	[36]
	SGA- LiCl-PVP	70°C, /	~0.5	~75%	~25	0.02	
MOFs	Co ₂ Cl ₂ BT DD	45°C, 5%RH	~0.8	~82%	~65	0.012	[29]
	MOF-333	85°C, 3%RH	~0.4	~93%	/	/	[27]
Carbon-based composites	Steam-80	62°C, /	~0.13	~99%	~10	0.013	[30]
Gel-based composites	PAETA- Ac	70°C, /	~0.4	~90%	~30	0.09	[31]

S2.15 AWH performance in the homemade device and cycling stability

The atmospheric water harvesting performance of PAM-LiCl was measured using a device as shown in Figure 4. Before the test, PAM-LiCl first was allowed to capture moisture for 4 hours at 20%RH to reach an equilibrium state with a water uptake of 1.1 g/g, i.e., the sorption process of the activation stage shown in Figure S21. PAM-LiCl was then placed into the AWE chamber for water release at 80°C for 30 minutes to complete the activation stage, where the water uptake decreased to ~0.5 g/g. Afterward, the AWH cycles were conducted by sorption at 20%RH for 70 minutes, followed by 30 minutes desorption at 80°C. An average net water uptake change (i.e., water release) of ~0.55 g/g and water collection of ~0.51 g/g can be obtained in each cycle. Benefiting from the fast sorption/desorption kinetics, PAM-LiCl could achieve 14 AWH cycles in one day, with a high daily water yield of ~ 7 g/g.

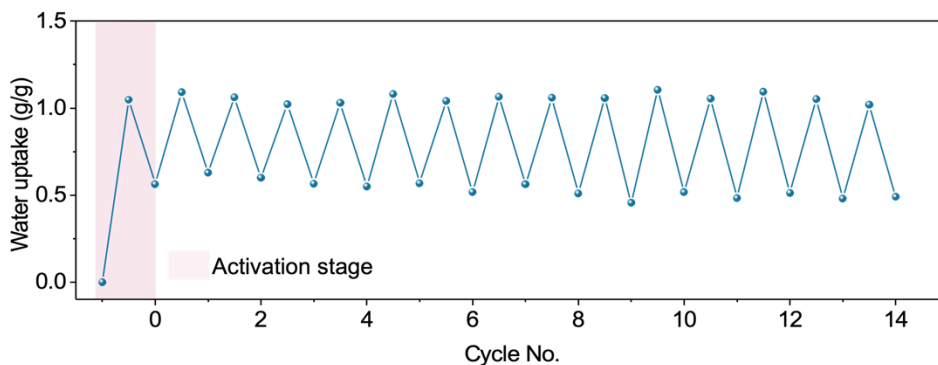


Figure S22. Water uptake of PAM-LiCl varying with AWH cycles. Pink region refers to the activation stage.

We conducted TGA and EDX of PAM-LiCl over cycles to investigate its cycling stability. As shown in Figure S23, after 15 cycles of sorption-desorption, PAM-LiCl shows a 67wt% LiCl content, which is very close to the initial state (68wt%). EDX mapping images of PAM-LiCl over cycles also showed that Cl is evenly distributed (Figure S24). These results confirmed the good durability of PAM-LiCl.

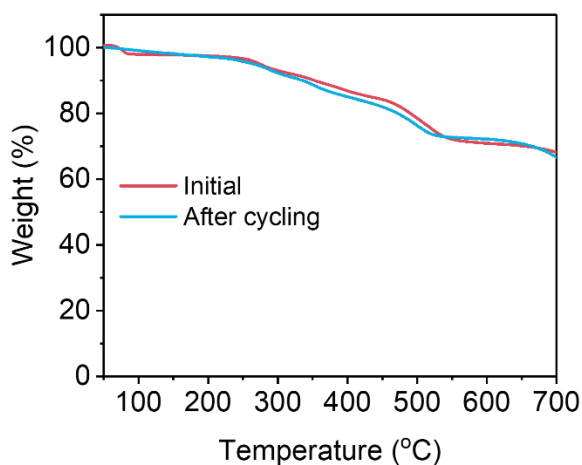


Figure S23. TGA curves of PAM-LiCl at the initial state and after 15 cycles.

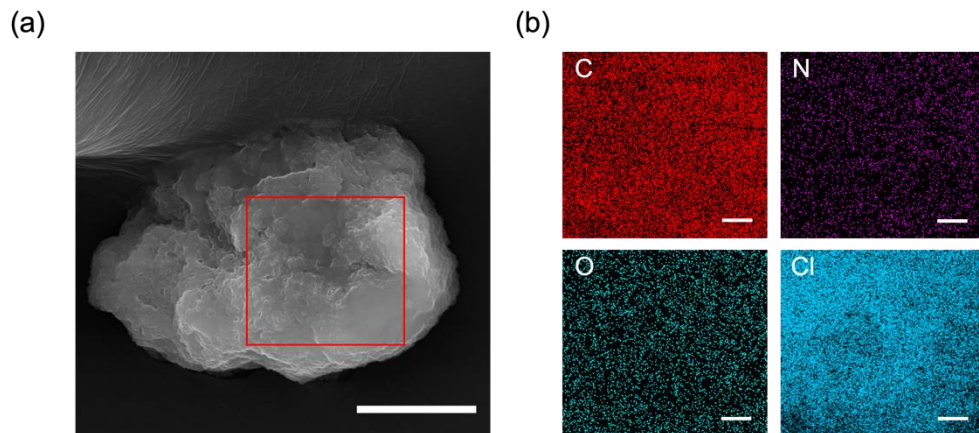


Figure S24. (a) SEM image and (b) EDX mapping images of PAM-LiCl after 15 sorption-desorption cycles. The red rectangle in (a) is the EDX mapping region. Scale bar: (a) 5 μ m; (b) 1 μ m.

We conducted the water collection experiment using a monolithic gel (2.5cm*3.5cm*0.08cm) of c.a. 200 mg (Figure S25b). Under each cycle of 70-minute sorption under 20%RH and 30-minute desorption at 80°C, average water uptake, water release and water collection of monolithic PAM-LiCl is 0.51 g/g, 0.47g/g and 0.41g/g, respectively (Figure S25c). Both water uptake and water release of monolithic sample is lower than those of powder sample, with average water uptake, water release and water collection of monolithic PAM-LiCl is 0.55 g/g, 0.55 g/g and 0.51g/g. As revealed in Figure S9, the monolithic sample shows lower sorption and desorption kinetics due to the smaller surface area.

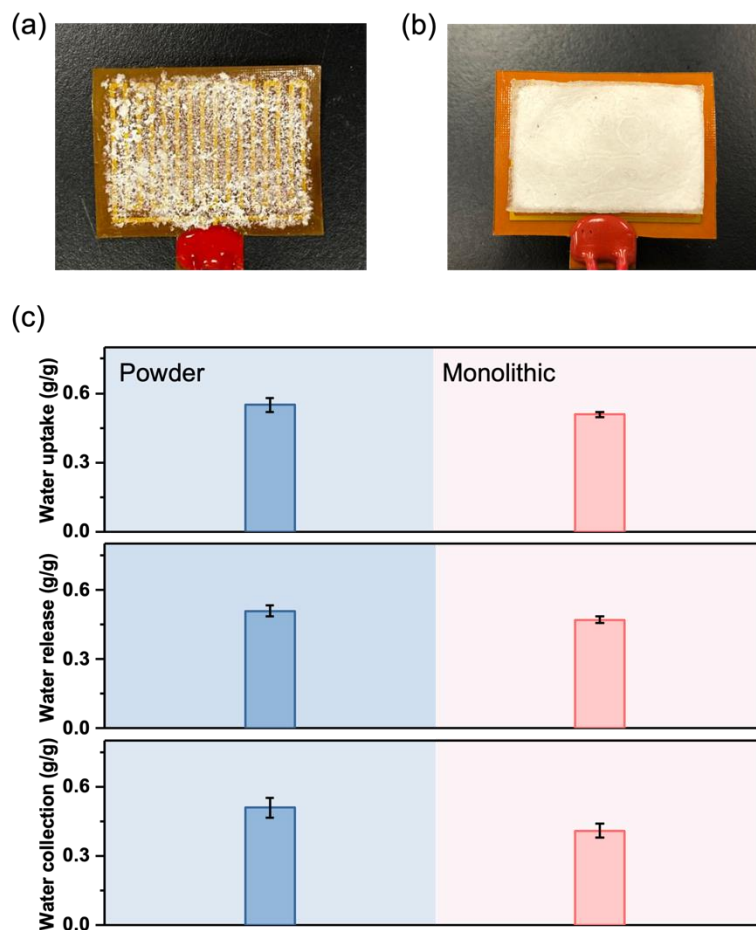


Figure S25. Photos of (a) powder and (b) monolithic PAM-LiCl on the heater (3*4 cm²). (c) Average water uptake, water release and water collection of each cycle of AWH experiment of powder and monolithic PAM-LiCl.

We further tested the AWH performance of PAM-LiCl at a large scale in another homemade device. As shown in Figure S26a, the AWH device consists of a larger AWH chamber, a thermocouple, and a power source. 1.2 g PAM-LiCl was attached to a heater for the large-scale AWH experiment (Figure S26b). As shown in Figure S26c, the average water uptake, water release, and water collection in each cycle of 1.2g PAM-LiCl are 0.52g/g, 0.49g/g, and 0.45g/g, respectively, which are very close to the performance based on 0.25 g sorbent (0.55 g/g water

uptake, 0.55 g/g water release, 0.51 g/g water collection). In summary, PAM-LiCl can maintain the water yield at a large scale in AWH applications.

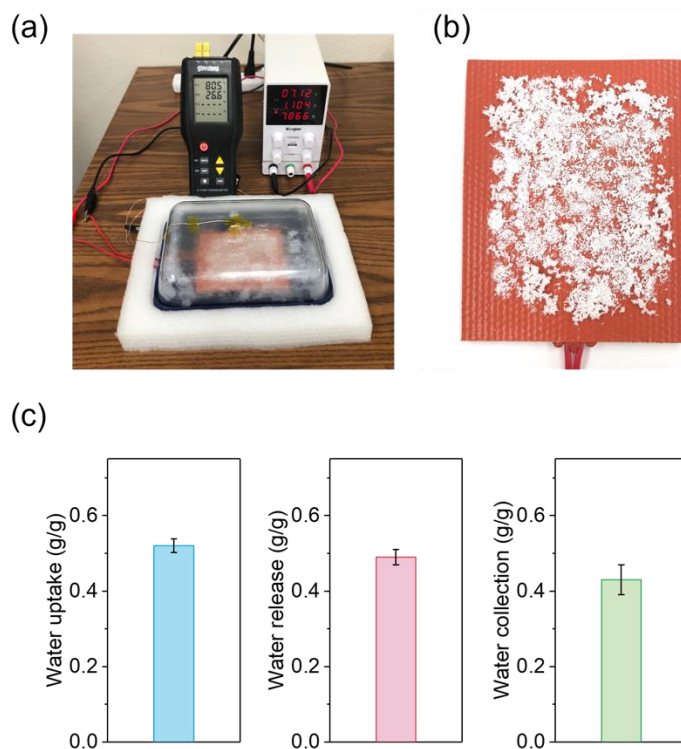


Figure S26. (a) Photo of AWH experiment setup for 1.2g PAM-LiCl including a water collection chamber, a thermocouple, and a power source. (b) Photo of 1.2g PAM-LiCl on a heater at a size of 10*12 cm². (c) Average water uptake, water release, and water collection in each cycle.

S2.16 Quality of collected water

We conducted ICP analysis on water harvested from PAM-LiCl to investigate the quality of the collected water. Li⁺ concentration is 0.32 mg/L and 0.26 mg/L in water collected from PAM-Li reaching equilibrium at 20%RH and 60%RH as representative RH for arid and humid regions, respectively (Figure S27). We assessed the quality of the collected water with the recommended Li-ion intake standard from 0.6 to 3.1 mg per day.^[37] According to the ICP results, the contents of

Li^+ in the collected water by PAM-LiCl during AWH at 20%RH and 60%RH are 0.32 mg/L and 0.26 mg/L, respectively. An adequate daily water intake is about 3.7L/day for males and 2.7L/day for females. Correspondingly, the Li^+ intake will be 0.962-1.184 mg/day for males and 0.702-0.864 mg/day for females. Therefore, water collected from PAM-LiCl is safe for human health.

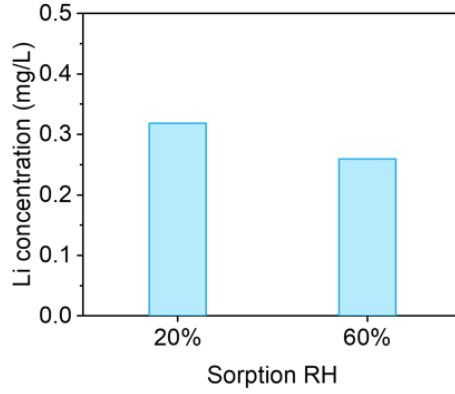


Figure S27. ICP analysis results showing LiCl concentration in water collected from PAM-LiCl after sorption at 20%RH and 60%RH.

S2.17 Energy analysis

The energy consumption during water release consists of latent heat and sensible heat, for the evaporation of water and heating of the sorbents, respectively. Latent heat, Q_l , is calculated from the equation,

$$Q_l = m_{sorbent} \Delta w Q_{de}$$

where $m_{sorbent}$ is weight of sorbent. Δw is the released water and Q_{de} is the heat of desorption.

Sensible heat, Q_s , can be computed by

$$Q_s = (C_{heater} m_{heater} + C_{sorbent} m_{sorbent} + C_{water} m_{sorbent} w)(T_d - T_s)$$

where C_{heater} , $C_{sorbent}$ and C_{water} is specific heat capacity of heater (main component of copper), sorbent and water, respectively. m_{heater} is weight of heater. T_d and T_s is the temperature of desorption and sorption.

The energy consumption, Q_c , normalized by the weight of the collected water is obtained by

$$Q_c = \frac{Q_t + Q_s}{m_{sorbent}\Delta w}$$

$$= \frac{m_{sorbent}\Delta w Q_{de} + (C_{heater}m_{heater} + C_{sorbent}m_{sorbent} + C_{water}m_{sorbent}w)(T_d - T_s)}{m_{sorbent}\Delta w}$$

By inputting values in into equation above, the energy consumption of PAM-LiCl and LiCl at water content of 1g/g can be obtained, as summarized in Table S4. The energy consumption of PAM-LiCl is 2877 J/g, lower than the 3234 J/g of LiCl.

The energy conservation, ΔQ , is thus calculated by

$$\Delta Q = Q_{c,LiCl} - Q_{c,PAM-LiCl}$$

According to equation above, the energy consumption per gram of collected water is 398 J/g, equal to 12% of the energy consumption of LiCl.

Table S4. Parameters and results of calculating energy consumption of PAM-LiCl and LiCl.

	PAM-LiCl	LiCl
$m_{sorbent}$ (g)	0.25	0.25
m_{heater} (g)	1.4784	1.4784
Δw (g/g)	1	0.76
w (g/g)	1	1

C_{sorbent} (J/(g K))	1.20	1.13
C_{heater} (J/(g K))	0.4	0.4
C_{water} (J/(g K))	4.2	4.2
Q_{de} (J/g)	2608	2945
T_{a} (K)	278	278
T_{d} (K)	353	353
Q_{c} (J/g water)	2836	3234

2.18 Cost analysis

PAM-LiCl is capable of good scalability for its facile fabrication process that relies on cost-efficient raw materials. As illustrated in S1.2 in SI, PAM-LiCl was prepared under room temperature and does not require high temperature or high pressure. The simple preparation also makes it easy to scale up PAM-LiCl. The total cost of PAM-LiCl is \$3.7/kg, with the cost of all raw materials listed in Table S4.

Table S5. Cost of large-scale production of PAM-LiCl.

Raw materials	Cost (\$/kg raw materials)	Material Consumption (kg/kg sorbent)	Material source
----------------------	-----------------------------------	---	------------------------

Acrylamide	1.8	0.39	https://www.alibaba.com/product-detail/Acrylamide-Solid-Acrylamide-98-_1600512021902.html?spm=a2700.galleryofferlist.normal_offer.d_title.5e9e70e9S6IkwJ&s=p)
LiCl	1	0.67	https://www.alibaba.com/product-detail/Industrial-Grade-desiccant-high-purity-99_1600415500102.html?spm=a2700.galleryofferlist.normal_offer.d_title.55e978e7mhw7QV&s=p)
Ammonium persulfate	0.4	0.02	https://www.alibaba.com/product-detail/Ammonium-Persulfate-New-Arrival-High-Purity_1600202350696.html?spm=a2700.galleryofferlist.normal_offer.d_title.35012c41s4w8yr&s=p)
N,N-tetramethylenediamine	195	1.1×10^{-5}	https://www.analytics-shop.com/us/sa-t22500-500ml-us.html?utm_source=google_shopping&utm_medium=cpc&gclid=Cj0KCQjwspKUBhCvARIsAB2IYusc4_2zC1m_OvE4G_lh5vt5s5PGJMTg8CccTlqrEyuFUDdJGFSe6gaAk3ZEALw_wcB)
N',N'-methylenebis(acrylamide)	4	0.03	https://www.alibaba.com/product-detail/Enough-stock-99-CAS-110-26_60831835953.html?spm=a2700.galleryofferlist.normal_offer.d_title.2a85187duGane2)

Supplementary references

- [1] A. P. Thompson, H. M. Aktulga, R. Berger, D. S. Bolintineanu, W. M. Brown, P. S. Crozier, P. J. in 't Veld, A. Kohlmeyer, S. G. Moore, T. D. Nguyen, R. Shan, M. J. Stevens, J. Tranchida, C. Trott, S. J. Plimpton, *Comput. Phys. Commun.* **2022**, 271, 108171.
- [2] J. Wang, R. M. Wolf, J. W. Caldwell, P. A. Kollman, D. A. Case, *J. Comput. Chem.* **2005**, 26, 114.
- [3] S. J. Rukmani, G. Kupgan, D. M. Anstine, C. M. Colina, *Mol. Simul.* **2019**, 45, 310.
- [4] I. S. Joung, T. E. Cheatham, *J. Phys. Chem. B.* **2008**, 112, 9020.
- [5] I. Pethes, *J. Mol. Liq.* **2018**, 264, 179.
- [6] H. W. Horn, W. C. Swope, J. W. Pitera, J. D. Madura, T. J. Dick, G. L. Hura, T. Head-Gordon, *J. Chem. Phys.* **2004**, 120, 9665.
- [7] J.-P. Ryckaert, G. Ciccotti, H. J. C. Berendsen, *J. Comput. Phys.* **1977**, 23, 327.
- [8] A. I. Jewett, D. Stelter, J. Lambert, S. M. Saladi, O. M. Roscioni, M. Ricci, L. Autin, M. Maritan, S. M. Bashusqeh, T. Keyes, R. T. Dame, J.-E. Shea, G. J. Jensen, D. S. Goodsell, *J. Mol. Biol.* **2021**, 433, 166841.
- [9] L. Martínez, R. Andrade, E. G. Birgin, J. M. Martínez, *J. Comput. Chem.* **2009**, 30, 2157.
- [10] T. Schneider, E. Stoll, *Phys. Rev. B* **1978**, 17, 1302.
- [11] H. J. C. Berendsen, J. P. M. Postma, W. F. van Gunsteren, A. DiNola, J. R. Haak, *J. Chem. Phys.* **1984**, 81, 3684.
- [12] W. G. Hoover, *Phys. Rev. A* **1985**, 31, 1695.
- [13] S. Nosé, *J. Chem. Phys.* **1984**, 81, 511.
- [14] S. Chowdhuri, A. Chandra, *Phys. Rev. E* **2002**, 66, 041203.
- [15] H. S. Sachar, B. S. Chava, T. H. Pial, S. Das, *Macromolecules* **2021**, 54, 2011.

- [16] Y. Tamai, H. Tanaka, K. Nakanishi, *Macromolecules* **1996**, 29, 6750.
- [17] R. Li, Y. Shi, M. Wu, S. Hong, P. Wang, *Nano Energy* **2020**, 67, 104255.
- [18] W. Wang, S. Xie, Q. Pan, Y. Dai, R. Wang, T. Ge, *Renew. Sustain. Energy Rev.* **2021**, 141, 110802.
- [19] P. A. Kallenberger, K. Posern, K. Linnow, F. J. Brieler, M. Steiger, M. Fröba, *Adv. Sustain. Syst.* **2018**, 2, 1700160.
- [20] J. Y. Wang, R. Z. Wang, Y. D. Tu, L. W. Wang, *Energy* **2018**, 165, 387.
- [21] R. Li, Y. Shi, M. Alsaedi, M. Wu, L. Shi, P. Wang, *Environ. Sci. Technol.* **2018**, 52, 11367.
- [22] A. Permyakova, S. Wang, E. Courbon, F. Nouar, N. Heymans, P. D'Ans, N. Barrier, P. Billefont, G. De Weireld, N. Steunou, M. Frère, C. Serre, *J. Mater. Chem. A* **2017**, 5, 12889.
- [23] C. Lei, Y. Guo, W. Guan, H. Lu, W. Shi, G. Yu, *Angew. Chem. Int. Ed.* **2022**, 61, e202200271.
- [24] P. A. Kallenberger, M. Fröba, *Commun. Chem.* **2018**, 1, 28.
- [25] J. Xu, T. Li, T. Yan, S. Wu, M. Wu, J. Chao, X. Huo, P. Wang, R. Wang, *Energy Environ. Sci.* **2021**, 14, 5979.
- [26] A. Cadiau, J. S. Lee, D. Damasceno Borges, P. Fabry, T. Devic, M. T. Wharmby, C. Martineau, D. Foucher, F. Taulelle, C.-H. Jun, Y. K. Hwang, N. Stock, M. F. De Lange, F. Kapteijn, J. Gascon, G. Maurin, J.-S. Chang, C. Serre, *Adv. Mater.* **2015**, 27, 4775.
- [27] N. Hanikel, X. Pei, S. Chheda, H. Lyu, W. Jeong, J. Sauer, L. Gagliardi, O. M. Yaghi, *Science* **2021**, 374, 454.
- [28] H. Furukawa, F. Gándara, Y.-B. Zhang, J. Jiang, W. L. Queen, M. R. Hudson, O. M. Yaghi, *J. Am. Chem. Soc.* **2014**, 136, 4369.

- [29] A. J. Rieth, S. Yang, E. N. Wang, M. Dincă, *ACS Cent. Sci.* **2017**, 3, 668.
- [30] Y. Song, N. Xu, G. Liu, H. Qi, W. Zhao, B. Zhu, L. Zhou, J. Zhu, *Nat. Nanotechnol.* **2022**.
- [31] M. Wu, R. Li, Y. Shi, M. Altunkaya, S. Aleid, C. Zhang, W. Wang, P. Wang, *Mater. Horiz.* **2021**, 8, 1518.
- [32] G. Yilmaz, F. L. Meng, W. Lu, J. Abed, C. K. N. Peh, M. Gao, E. H. Sargent, G. W. Ho, *Sci. Adv.* **2020**, 6, eabc8605.
- [33] T. Nakaoki, H. Yamashita, *J. Mol. Struct.* **2008**, 875, 282.
- [34] W. B. Monosmith, G. E. Walrafen, *J. Chem. Phys.* **1984**, 81, 669.
- [35] J. Xu, T. Li, J. Chao, S. Wu, T. Yan, W. Li, B. Cao, R. Wang, *Angew. Chem. Int. Ed.* **2020**, 59, 5202.
- [36] A. Entezari, M. Ejeian, R. Wang, *Appl. Therm. Eng.* **2019**, 161, 114109.
- [37] G. N. Schrauzer, *J. Am. Coll. Nutr.* **2002**, 21, 14.